Role of spanwise rollers by Kelvin–Helmholtz instability in turbulence over a permeable porous wall

Role of spanwise rollers by Kelvin–Helmholtz instability in turbulence over a permeable porous wall

Yusuke Kuwata *

Department of Mechanical Engineering, Osaka Prefecture University, 1-1 Sakai, Osaka 599-8531, Japan

(Received 10 February 2022; accepted 29 July 2022; published 22 August 2022)

Direct numerical simulations of porous-walled channel flows with computational domain size constraints were performed to clarify the role of spanwise rollers associated with the Kelvin–Helmholtz instability on turbulent flows over a porous wall. The constraints of the domain size, which effectively hindered the development of the spanwise roller sustaining the near-wall turbulent motions, were imposed to isolate the effects of the near-wall turbulent motions and spanwise rollers. For each domain case, we considered thick and thin porous walls to isolate the effects of surface roughness and vertical permeability. It is found that the surface roughness plays a principal role in the modification of near-wall turbulent motions, including streaks and longitudinal vortices, whereas vertical permeability is essential for the development of spanwise rollers with streamwise alternating low- and high-speed regions. The spanwise roller contributes to an increase in the skin friction coefficient at the porous wall, and considerably increases the turbulence intensities deep inside the porous wall. The discussion in the logarithmic region based on the extended Jackson model reveals that the von Kármán constant is increased in the presence of the spanwise rollers, which is considered to reflect an increase in the characteristic vortex size owing to the spanwise rollers. The increase in the mixing length due to the role of the spanwise roller can be reasonably predicted by the classical mixing-length model with an increased von Kármán constant.

DOI: 10.1103/PhysRevFluids.7.084606

I. INTRODUCTION

A turbulent flow over permeable porous walls is a problem inherent to many engineering applications of interest because porous media have a large contact area per volume, enabling considerable heat and mass transfer. Porous media have applications in numerous fields of engineering, such as in gas diffusion layers in proton exchange membrane fuel cells, catalytic converters for automobile exhaust systems, transpiration cooling systems, and heat exchangers. In addition, in the context of the geophysical and environmental fields, the flows over vegetation and urban canopies and natural river beds can also be categorized as porous wall turbulence. In studies on turbulent flows around porous media, particular interest is focused on the effect of characteristics of porous media on turbulent boundary layers over a porous wall because the modification of turbulence strongly depends on characteristics of porous media.

One of the primary interests of turbulent boundary layers with porous walls is the penetration effect of flows inside a porous wall. The enhanced momentum exchange across the porous wall interface is not only due to turbulence enhancement by surface roughness but also due to the relaxation of the wall-blocking effects. To quantify flow penetration inside a porous wall, the permeability tensor is commonly used, which is defined in the convection theory for porous medium flow proposed

*kuwata@me.osakafu-u.ac.jp

by Darcy [1]. For isotropic porous media in which the diagonal components of the permeability tensor are the same, numerical and experimental studies [2–6] reached the same conclusion that the turbulence over a porous medium wall is enhanced with increasing wall permeability. The experiments of turbulent flows over ceramic foams with different permeabilities by Suga *et al.* [3] revealed that the parameters related to the logarithmic mean velocity profiles are closely associated with the permeability Reynolds number, which is supported by other experimental studies [5] and direct numerical simulation (DNS) studies [7,8]. For anisotropic porous media, Kuwata and Suga [7] reported that the streamwise component of a permeability tensor plays a crucial role in turbulence enhancement rather than the wall-normal component. Conversely, Gómez-de-Segura *et al.* [9] and Rosti *et al.* [10] reported that turbulence reduction can be achieved for the streamwise preferential permeable walls with an excessively low wall-normal permeability because such porous walls induce slip velocity at the porous/fluid interface with a suppression of the turbulent eddy penetration.

Another interesting characteristic of porous wall turbulence is the presence of spanwise rollers, which has received much attention over the past decades [2,11–14]. Previous experimental studies on the role of the spanwise roller in canopy turbulence in Refs. [11,12] showed that the flow over vegetation canopies behaves as a plane-mixing layer rather than a boundary layer because of the presence of the Kelvin–Helmholtz (K–H) type of instability originating at an inflectional point of the streamwise mean velocity. This mixing layer hypothesis provides a reasonable explanation for the many distinctive features of canopy turbulence, including turbulent transport, sweep and ejection motions, and turbulent length scales. However, owing to a limitation of the available data for experiments, a full appreciation of the characteristics of the spanwise roller is not possible. Thus, DNS may be an alternative tool to shed light on the nature of the spanwise roller.

The DNSs with modeled porous walls in Refs. [2,15,16] confirm that turbulent flows over highly permeable porous walls are dominated by relatively large-scale turbulent motions associated with the spanwise rollers. The presence of the spanwise rollers has also been identified in DNSs with resolved porous walls [6–8,17,18]. Kuwata and Suga [6,17] demonstrated that the turbulence near the porous wall is characterized by streamwise alternating high- and low-speed regions modulated by the spanwise rollers. This turbulent motion delivers energy to the porous wall through pressure diffusion, thereby enhancing turbulence inside the porous wall [2,17,18]. Furthermore, the enhanced redistribution process increases the wall-normal Reynolds stress over the porous wall, which, in turn, strengthens the Reynolds shear stress [17].

Regarding the length scale of the spanwise roller, Refs. [7,8,19] reported that the characteristic wavelength of the streamwise perturbation modulated by the spanwise rollers was approximately three to five times as large as the boundary layer thickness. Although the characteristic length scale depends on its determination procedure to a certain extent, other DNS studies [2,15,18] also showed that the characteristic length was of the order of several boundary layer thicknesses. The similar conclusion was drawn for the open channel flow over gravel beds [20,21]. For a canopy flow, which behaves quite similar to the plane-mixing layer rather than the boundary layer, Raupach *et al.* [12] reported that the wavelength of the spanwise roller can be scaled by the shear layer thickness, which is analogous to the vorticity thickness for the plane-mixing layer. This shear length scale has the same order of the boundary layer thickness for aquatic vegetation, whereas it is comparable to the canopy height for a terrestrial canopy where the canopy turbulence is unconfined [12,22].

The DNS and experimental studies have reached a consensus that the spanwise rollers associated with the K-H instability play a vital role in the turbulence and momentum transport across the porous/fluid interface. However, the turbulent flows over porous walls include near-wall turbulent vortices as well as relatively large-scale spanwise rollers, both of which are expected to be affected by the surface roughness and wall permeability. This complexity makes it difficult to identify the role of the spanwise rollers and the effects of the surface roughness and wall permeability. The goal of this study is to identify the role of the spanwise rollers associated with K-H instability and clarify how surface roughness and wall permeability alter turbulent flows over porous walls. Specifically, this study focuses on the effects of the vertical permeability of an isotropic porous medium, which

are related to the wall-blocking effects of near-wall turbulence [3]. To this end, a series of DNSs of porous-walled channel flows with computational domain size constraints was performed for thick and thin porous walls. A thin porous wall over an impermeable solid wall was used to isolate the effects of the surface roughness and vertical permeability, as in Refs. [6,23,24]. For the constraints of the domain size, we considered the streamwise- and spanwise-reduced domains to artificially manipulate the spanwise rollers. The streamwise-reduced domain was designed such that the spanwise rollers do not develop over a porous wall, whereas the spanwise-reduced domain generates artificially enhanced spanwise rollers owing to an insufficient spanwise domain.

II. NUMERICAL METHOD

In this study, DNSs were performed using the lattice Boltzmann method (LBM) where the time evolution of the particle density distribution functions was solved based on the gas kinetic theory. The governing equation of the LBM is the lattice Boltzmann equation, which is proven to recover the continuity and Navier-Stokes equations in second-order accuracy in space and time. The nature of its low numerical dissipation and dispersion leads to success in the LBM-DNS of canonical turbulent flows [25–27]. Notably, the separation of the local and nonlocal computations offers a significant advantage over conventional computational fluid dynamic solvers in terms of the efficiency of parallel computation [28–30]. Furthermore, LBM is particularly suitable for dealing with a flow in a complicated geometry because of the considerable simplicity and high accuracy of curved wall treatments. The above-mentioned advantages motivate us to perform LBM-DNS of complex turbulent flow problems, such as flows over and/or inside porous media [6,31,32], flows over rough walls [33–36], and particle-laden flows [37–39].

For three-dimensional flow simulations using the LBM, there are several possible choices for discrete velocity models and collision operations. Following previous DNS studies by the author's group [6,7,35,40], we chose the D3Q27 multiple-relaxation-time lattice Boltzmann method (MRT-LBM), in which the lattice Boltzmann equations are discretized into 27 discrete velocity components and each moment is relaxed toward the equilibrium state with optimized relaxation factors (a full description of the numerical method is provided in Ref. [26]). Note that the MRT-LBM was rigorously validated through turbulent channel and pipe flows [26], and has been successfully applied to turbulent flows over porous and rough walls [35,40–42]. Indeed, the present numerical scheme produced results in excellent agreement with the experimental data for turbulent flows in a porous medium [26], in a porous-walled channel [7], and in a square duct partially filled with a rod array [42].

III. FLOW CONFIGURATION AND COMPUTATIONAL DETAILS

A. Flow geometry

The configuration of a porous-walled channel flow is presented in Fig. 1, where H and h are the channel and porous wall heights, respectively. An impermeable solid wall was considered for the top and bottom walls at $y = H$ and $y = -h$, respectively, whereas the porous wall in $-h < y < 0$ was modeled as arrays of Kelvin cells (polyhedron with six square faces and eight hexagonal faces [43]). The flow was periodic in the streamwise (x) and spanwise (z) directions. A streamwise pressure difference was prescribed to drive the flow. For the baseline case, the computational domain of $L_x(x) \times (H + h)(y) \times L_z(z)$ with $L_x = 6H$ and $L_z = 3H$ was considered, and the porous wall thickness was given as $h = H$, which is sufficient to neglect the effect of the bottom wall [6,7]. Note that the domain size of the baseline case is the same as or larger than those used in the previous DNS studies [2,6–8,15,44]. Kuwata and Suga [7] reported that this domain size adequately captured spanwise rollers due to K-H instability, and doubling the domain size in the x and z directions yielded a negligible change in the turbulence statistics.

In this study, the effects of the spanwise rollers arising from K-H instability were examined by controlling the spanwise rollers with the constraints of the computational domain and the porous

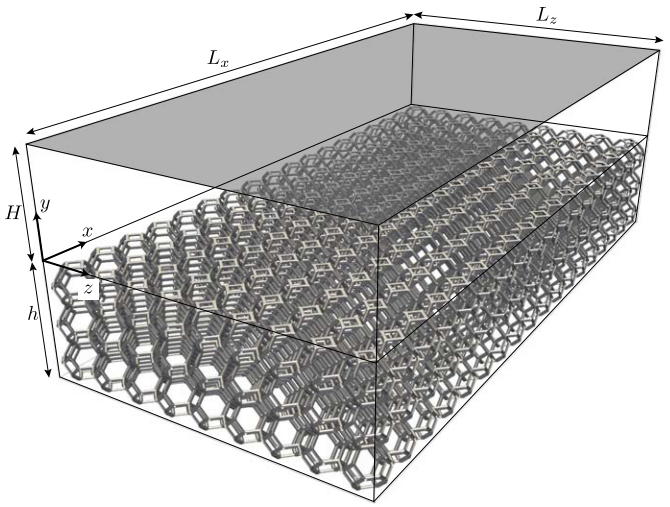

FIG. 1. Configuration of a porous-walled channel flow.

wall thickness. As for the computational domain, we additionally considered the streamwise-reduced domain by a factor of 6 ($L_x = H$) and the spanwise-reduced domain by a factor of 3 ($L_z = H$). Because the size of the reduced domains was sufficiently large to capture the minimal flow unit of the near-wall turbulent vortices [45], the near-wall structures including streaks and longitudinal vortices were sustained for the reduced domain. Nevertheless, as the domain size was too small to properly accommodate the spanwise rollers, the spanwise rollers were not developed for the streamwise-reduced domain but artificially enhanced for the spanwise-reduced domain, which will be discussed in Sec. IV A. This enables us to discuss the isolated role of near-wall turbulent vortices and the spanwise rollers. Following the studies in Refs. [6,23,24], two porous wall thickness cases were considered for each case to isolate the effects of surface roughness and vertical permeability: one was the case with $h = H$, and the other was the case with $h = H/3$. For the thin porous wall cases, the vertical turbulent flow motion across the porous/fluid interface is attenuated by the solid wall beneath the porous wall, resulting in a reduction in vertical permeability. Note, however, that it is difficult to perfectly distinguish between the effects of surface roughness and permeability. The effects of porous and rough walls are usually modeled as in a similar manner in the framework of the spatially averaged Navier-Stokes equation [2,46,47]. Consequently, we considered six simulation cases with different computational domain sizes and porous wall thickness, as shown in Fig. 2. In the following, for the sake of brevity, cases were named according to *A*x*B*z-*C*, where $A = L_x/H$ is the streamwise domain length, $B = L_z/H$ is the spanwise domain length, and C is either "thin" ($h = H/3$) or "thick" ($h = H$), as shown in Fig. 2.

B. Porous medium

To mimic the porous foam, the porous wall was modeled as a regular structure with a so-called Kelvin cell [43]. The Kelvin cell structure is commonly used for modeling porous media [48–52]. It was reported that the hydrodynamic characteristics of the Kelvin cell were similar to those of a real porous foam [49,52]. Figure 3 depicts a single unit of the Kelvin cell used in this study. A circular cylinder was considered for the ligament of the Kelvin cell structures, and the diameter of the cylinder, D, was adjusted such that the porosity of the Kelvin cell becomes $\varphi = 0.95$, assuming a high-porosity metal [53]. Here, the porosity φ is defined as the ratio of the fluid phase volume V_f occupied within the unit cell to the volume of the unit cell, $V = L^3$, that is, $\varphi = V_f/V$. The resulting diameter is $D = 0.0909L$, where L is the size of the Kelvin cell. In the present coordinate system,

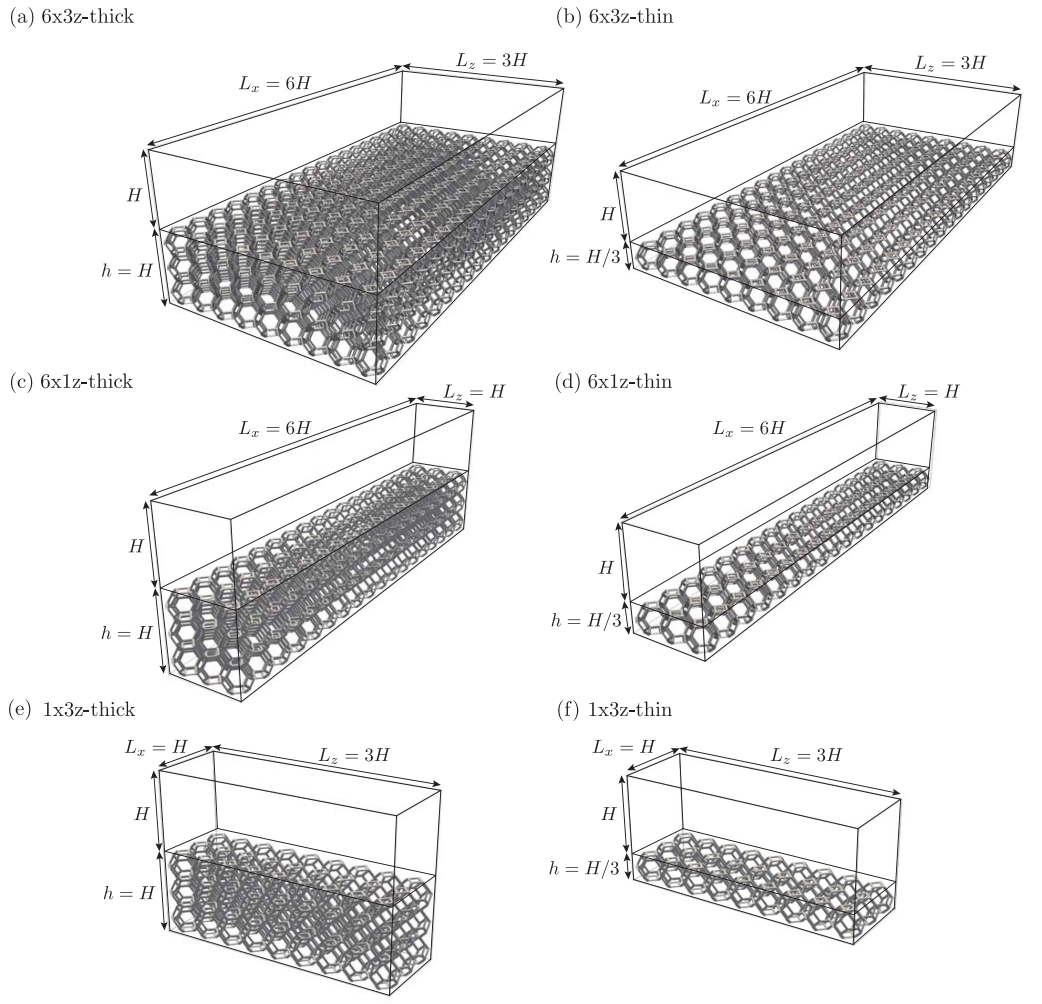

FIG. 2. Flow geometry of the DNSs: (a) case 6x3z-thick, (b) case 6x3z-thin, (c) case 6x1z-thick, (d) case 6x1z-thin, (e) case 1x3z-thick, and (f) case 1x3z-thin.

as shown in Fig. 3, the diagonal components of the permeability tensor of the Kelvin cell are the same, $K = K_{11} = K_{22} = K_{33}$, and the off-diagonal components $K_{ij} = 0$ $(i \neq j)$ are zero.

A preliminary simulation of the fully developed porous medium flows yielded the permeability of $K/L^2 = 1.7 \times 10^{-2}$. The size of the single unit of the Kelvin cell was set to $L = H/3$ as shown in Fig. 1. Hence, the thick porous wall was composed of three Kelvin cell layers as shown in Figs. 2(a), 2(c), and 2(e), whereas a single Kelvin cell layer was used for the thin porous wall as shown in Figs. 2(b), 2(d), and 2(f). The total number of Kelvin cells for the baseline case of 6x3z-thick results in $18(x) \times 3(y) \times 9(z)$. The single unit of the Kelvin cell was resolved by 110 grid points along each direction, and the cross section of the circular ligament was resolved by approximately 10×10 grids.

C. Flow conditions and computational details

We conducted simulations using a fixed streamwise pressure difference so that the friction Reynolds number based on the average friction velocity u_τ and channel height H was $\mathrm{Re}_\tau = 630$

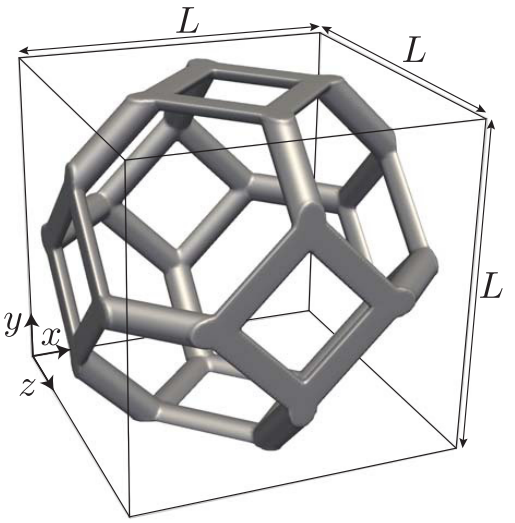

FIG. 3. A single unit of the Kelvin cell structure.

(the definition of u_τ is presented in Sec. III E). In terms of the computational grid, the LBM is generally discretized with the equal spacing regular grid, which requires prohibitively high computing resources for handling the entire computational domain with a sufficiently fine grid resolution. To resolve this problem, we applied the local grid refinement technique proposed by Kuwata and Suga [54] as in previous DNSs [6–8,35,41]. We allocated a doubly refined grid around the porous wall of $-h < y < 0.14H$ to properly resolve the geometry of the porous wall and fine-scale eddy motions above the porous wall. Note that the grid interface position of $y = 0.14H$ corresponds to approximately 100 porous wall units off from the porous wall, where the porous wall unit is defined as ν/u_τ^p with u_τ^p being the friction velocity at the porous wall (see Sec. III E for the definition of u_τ^p).

The grid resolution near the porous wall was determined such that the grid spacing was approximately 2 porous wall units, as in the previous lattice Boltzmann DNS studies by Kuwata and Suga [6]. The resulting total number of grid points for the baseline case (6x3z-thick) is approximately 8×10^8. The grid resolution is comparable to that in the geometry-resolved porous or rough wall turbulence DNSs with the same numerical scheme [6,7,35,40,42,55]. Hence, the grid resolution is expected to be sufficiently fine to resolve fine-scale eddies and complicated wall geometries. Nevertheless, to establish grid independence, we conducted a grid sensitivity study. A comparison between the results with the resolutions of 1.8 and 2.4 porous wall units confirmed that relative differences in the local mean velocity and streamwise turbulence intensity profiles were at most 0.7% and 3.7%, respectively. The difference in the skin friction coefficient was found to be approximately 0.5%.

D. Averaging procedure

Unlike DNSs with volume-averaged governing equations with the prescribed drag force model [2,9,10,56], we exactly resolved the geometry of the porous wall, resulting in spatially inhomogeneous turbulence statistics in the x-z plane near the porous wall. To statistically discuss flows from a macroscopic viewpoint, we introduce spatial averaging. For spatial averaging, it is common to employ volume averaging [44,57]. However, for the thin porous wall cases, there is no sufficient scale separation between the porous wall thickness h and the size of the volume of averaging (representative elementally volume), L, that is, $h = L$. This makes it impossible to obtain profiles

of volume-averaged values inside the porous wall. Therefore, in this study, we alternatively discuss the variable averaged over the x-z plane as follows [6]:

$$\langle\phi\rangle(y,t) = \frac{1}{A}\int_{x_f}\int_{z_f}\phi(x,y,z,t)dxdz, \quad \langle\phi\rangle^f(y,t) = \frac{1}{A_f(y)}\int_{x_f}\int_{z_f}\phi(x,y,z,t)dxdz, \tag{1}$$

where x_f and z_f denote the positions of the fluid phase, and $\langle\phi\rangle$ and $\langle\phi\rangle^f$ represent the superficial and intrinsic (fluid phase) averaged values, respectively. Intrinsic averaging is the averaging over the x-z plane occupied by the fluid phase. The plane porosity is $\varphi(y) = A_f(y)/A$, where $A = L_xL_z$ is the x-z plane area, and $A_f(y)$ is the fluid phase area containing a certain x-z plane. The dispersion from the intrinsic averaged value is denoted by $\tilde{\phi} = \phi - \langle\phi\rangle^f$.

In addition, as the variable also fluctuates in time, we consider Reynolds averaging. The Reynolds-averaged value of a variable ϕ is denoted as $\overline{\phi}$, and ϕ' denotes the fluctuation from the Reynolds-averaged value: $\phi' = \phi - \overline{\phi}$. For Reynolds averaging, statistical variables are assembled over a period of $600T$ (where $T = H/U_b$ is the convection time), after the flow has reached a fully developed state. Note that the bulk mean velocity U_b is defined as $U_b = Q_c/H$, where Q_c is the flow rate in the clear flow region of $y > 0$.

E. Flow characteristic parameters

For the present flow configuration, in which the flow is bounded by a porous and solid wall, the friction velocity is not unique. For the top solid wall, we can directly compute the wall shear stress at the wall, τ_w^s, and the friction velocity at the solid wall is simply given as $u_\tau^s = \sqrt{\tau_w^s/\rho}$. For the wall shear stress at a porous wall, following Refs. [6,8,47], we computed the average wall shear stress at the porous wall from the streamwise momentum balance between the pressure drop ΔP and the averaged wall shear stress $\tau_w^p = \rho(u_\tau^p)^2$ as follows:

$$L_xL_z\left(\tau_w^p + \tau_w^s\right) = HL_z\Delta P. \tag{2}$$

This yields

$$\tau_w^p = H\frac{\Delta P}{L_x} - \tau_w^s. \tag{3}$$

In this study, we performed simulations with a constant streamwise pressure difference; i.e., the averaged wall shear stress $\tau_w = (\tau_w^p + \tau_w^s)/2$ is fixed as

$$\tau_w = \frac{H}{2}\frac{\Delta P}{L_x}. \tag{4}$$

The wall shear stress at the porous wall, τ_w^p, defined in Eq. (3) corresponds to the total shear stress at the porous/fluid interface. This definition is consistent with those used in the canopy flow [13,58] and porous-walled channel flow [2,3,6]. In what follows, the superscripts "$()^{p+}$" and "$()^+$" stand for the value nondimensionalized with u_τ^p and u_τ, respectively.

A difference in the wall conditions for the top and bottom walls resulted in an asymmetry of the mean velocity profile in the clear flow region of $0 < y < H$. This leads to different boundary layer thicknesses for the porous and top wall sides. The boundary layer thickness for the porous wall side is defined as the distance from the porous/fluid interface to the location where the total shear stress becomes zero as in Ref. [2]. Given that the total shear stress profiles are linear in terms of y, the boundary layer thicknesses for the porous δ_p wall side is given as follows:

$$\delta_p = \frac{\tau_w^p}{\tau_w^s + \tau_w^p}H. \tag{5}$$

TABLE I. Flow characteristics of the simulation. The skin friction coefficient at the porous wall, $C_f^p = \tau_w^p/(0.5\rho U_b^2)$, that at the solid wall, $C_f^s = \tau_w^s/(0.5\rho U_b^2)$, the ratio of the wall shear stress at the porous wall to that at the solid wall, τ_w^p/τ_w^s, the streamwise length in wall units, L_x^{p+}, and the spanwise length in wall units, L_z^{p+}, are included.

Case	$C_f^p(\times 10^{-2})$	$C_f^s(\times 10^{-2})$	τ_w^p/τ_w^s	L_x^{p+}	L_z^{p+}
1x3z-thin (streamwise reduced)	2.7	0.99	2.7	760	2279
6x1z-thin (spanwise reduced)	2.7	0.98	2.7	4562	760
6x3z-thin (full)	3.3	1.05	3.1	4646	2323
1x3z-thick (streamwise reduced)	2.7	0.99	2.7	760	2279
6x1z-thick (spanwise reduced)	5.1	1.16	4.4	4819	803
6x3z-thick (full)	4.7	1.24	3.8	4760	2380

IV. RESULTS AND DISCUSSIONS

A. Global flow characteristics

Before discussing profiles of the turbulence statistics, we first discuss the flow characteristic parameters and the inner-scaled domain size in Table I, where the skin friction coefficient at the porous wall is $C_f^p = \tau_w^p/(0.5\rho U_b^2)$, that at the solid wall is $C_f^s = \tau_w^s/(0.5\rho U_b^2)$, the ratio of the wall shear stress at the porous wall to that at the solid wall is τ_w^p/τ_w^s, the streamwise length in wall units is L_x^{p+}, and the spanwise length in wall units is L_z^{p+}. For all cases, the wall shear stress at the porous wall is several times as large as that at the solid wall ($\tau_w^p/\tau_w^s = 2.7$–4.4), which is considered to be due to the role of surface roughness as well as wall permeability. Note that the permeability Reynolds number is approximately $\mathrm{Re}_K = u_\tau^p\sqrt{K}/\nu \simeq 33$, and this value is much higher than the threshold value of 3.0 [3], suggesting that the wall permeability under consideration is sufficiently large to affect turbulence over a porous wall. Regarding the computational size for the reduced-domain cases, the inner-scaled spanwise and streamwise lengths are $L_z^{p+} = 760, 803$ (cases 6x1z) and $L_x^{p+} = 760$ (cases 1x3z), respectively. This is sufficiently large to capture the minimal flow unit [45]; the minimal spanwise extent that can capture a single set of wall structures is approximately 100 wall units, whereas the minimal streamwise period is within the range of approximately 250–350 wall units. Still, the reduced domain sizes are too small to properly reproduce the turbulence in the logarithmic region [59–62].

For the thin porous wall cases, C_f^p for the reduced-domain cases (1x3z and 6x1z) are similar and are 24% lower than that for the full-domain case (6x3z). The lower skin friction coefficient value for the reduced-domain cases can also be found for C_f^s, and this is owing to the insufficiency of the domain size in the logarithmic region. Indeed, Jiménez and Moin [45] and MacDonald *et al.* [61] reported that insufficient domain size results in an unphysical increase in the inner-scaled mean velocity in the wake region, leading to a decrease in the skin friction coefficient.

For the thick porous wall cases, the thickening of the porous wall has little effect on C_f^p for the streamwise-reduced domain cases (1x3z), whereas it considerably increases C_f^p for the spanwise-reduced domain (6x1z) and full-domain (6x3z) cases. Specifically, C_f^p is increased by 93% for cases 6x1z and 43% for cases 6x3z. Interestingly, thickening of the porous wall also increases C_f^s for the spanwise-reduced (6x1z) and full-domain (6x3z) cases. A possible explanation for the increase in C_f^p is the role of the spanwise rollers associated with K-H instability, and an increase in C_f^s indicates that the influence of spanwise rollers extends beyond the boundary layer over the porous wall, as reported by Kuwata and Suga [8]. There are several necessary conditions for the development of the spanwise rollers, such as an inflectional point of the mean velocity profiles [12,15], a sufficient depth of porous walls [6], and a sufficient domain size to accommodate the spanwise rollers. For case 1x3z-thick, the streamwise length of $L_x/\delta_p \simeq 1.4$ does not satisfy the requirement for the domain size because this

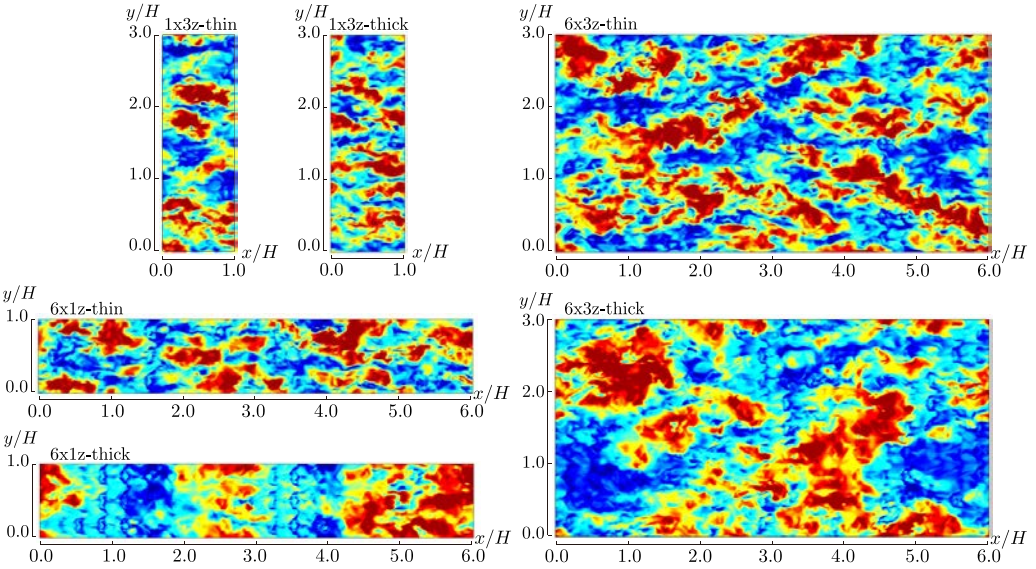

FIG. 4. Snapshots of the streamwise velocity fluctuations normalized by u_τ^p in the x-z plane at $y^{p+} \simeq 10$.

is much shorter than the characteristic wavelength of the spanwise roller $\lambda_x/\delta_p = 3$–5.5 [7,8,19]. Therefore, it is conjectured that the spanwise rollers can develop only for cases 6x3z-thick and 6x1z-thick, which may be the primary reason for the considerable increases in C_f for these cases. However, care should be taken when discussing the requirement for the domain size to accommodate the spanwise rollers because the reduced domains do not yield a physically correct value for δ_p. We will discuss the presence of the spanwise roller in the following section.

B. Flow structures

To obtain a physical understanding of the modification of C_f^p, we now discuss the flow structures around thin and thick porous walls. Figure 4 presents snapshots of the streamwise velocity fluctuations normalized by u_τ^p above the porous wall at $y^{p+} \simeq 10$. For the streamwise-reduced cases 1x3z, no distinct difference in the turbulence structures between the thin and thick porous wall cases is observed. In contrast, for the spanwise-reduced cases of 6x1z, a clear difference is detectable between the thin and thick porous wall cases. For the thick porous wall case (6x1z-thick), the streamwise elongated wall structure is absent, and the turbulence structure is organized into streamwise alternating low- and high-speed regions. This streamwise perturbation is responsible for the spanwise rollers associated with the K-H instability [2,6,13–15]. For the full-domain cases of 6x3z-thick, we cannot observe such a distinct streamwise perturbation. However, the turbulence structure for case 6x3z-thick is characterized by the relatively larger high- and low-speed regions which have a connection in the spanwise direction rather than in the streamwise direction. This turbulence structure is similar to that observed in DNSs on porous wall turbulence [2,6,8]. Hence, the turbulence structure for case 6x3z-thick may be a signature of the spanwise rollers by the K-H instability.

The spanwise roller structure associated with the streamwise perturbation by K-H instability can also be identified from snapshots of the pressure fluctuations along with the fluctuating velocity vectors for the full-domain cases in Fig. 5 where the velocity and pressure fluctuations are averaged over the spanwise direction. Here, spanwise averaging is taken in order to diminish the fine-scale turbulent motions, highlighting the fluctuations associated with the streamwise perturbations modulated by the spanwise rollers [19]. Apparently, for thick porous wall cases of 6x3z-thick in Fig. 5(a),

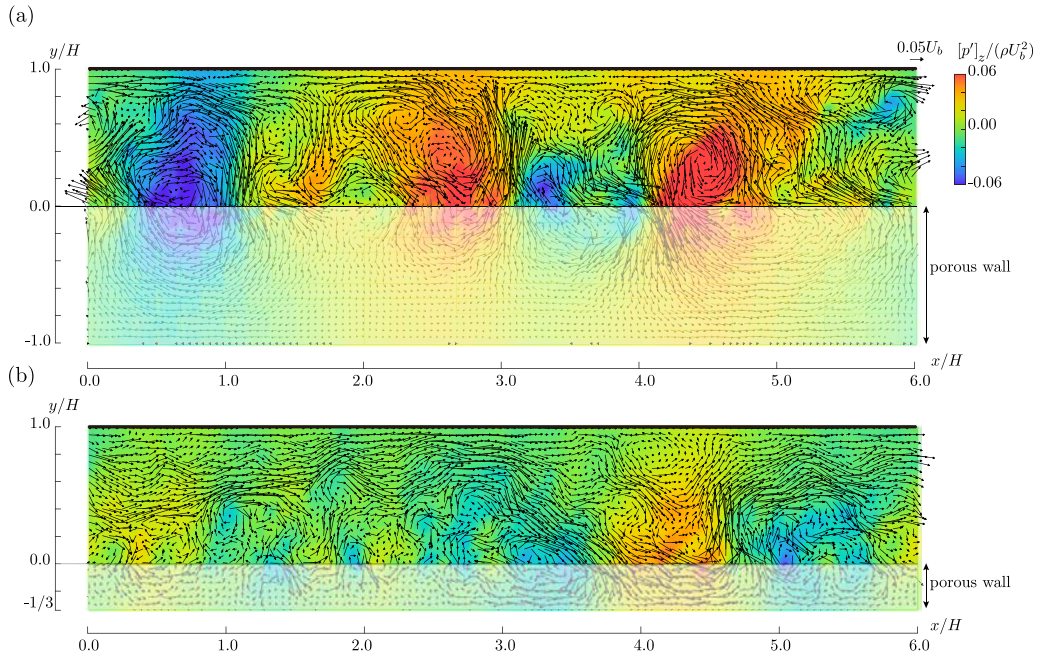

FIG. 5. Snapshots of the pressure fluctuations along with the fluctuating velocity vectors for (a) case 6x3z-thick and (b) case 6x3z-thin. Here, $[p']_z$ in the figure indicates spanwise-averaged pressure fluctuations, and spanwise averaging is also considered for the fluctuating velocity vectors.

the high- and low-pressure regions alternatively appear with the spanwise rollers. The flows are dominated by intensified downwash and upwash flows accompanied by the spanwise rollers, which may affect flows proximate to the top solid wall as well as the flows deep inside the porous wall. As shown in Table I, the thickening of the porous wall modifies the skin friction coefficient at the solid wall; i.e., C_f^s for case 6x1z-thick is 18% larger than that for case 6x1z-thin. This agrees with the findings in Ref. [8] that the influence of the spanwise rollers by K-H instability was not confined near the porous wall but extends beyond the boundary layer over the porous wall. In contrast, for the thin porous wall cases as shown in Fig. 5(b), no such spanwise rollers are visible, and the pressure fluctuations are much weaker in comparison with the thick porous wall case. These observations confirm that the spanwise rollers develop only for the thick porous wall cases.

To quantitatively discuss the flow structure over the porous walls, Fig. 6 presents two-dimensional premultiplied spectra of streamwise velocity fluctuations over the porous walls at $y^{p+} \simeq 10$. It is evident from Fig. 6(a) that for the streamwise-reduced domain (1x3z) cases, the porous wall thickness has little effect on the energy spectra. Considering that the spanwise roller is absent for these cases, we can conclude that the near-wall turbulent motions related to the streaks and longitudinal vortices are predominantly altered by surface roughness rather than vertical permeability. Conversely, for the other cases of 6x1z and 6x3z in Figs. 6(b) and 6(c), the energy spectra for the thick porous wall case is quite different from that for the thin porous wall case. For the thick porous wall cases, the energy spectra for the longer wavelength region become more energetic. The maximum peak location for the energy spectra for the full domain (6x3z) is $(\lambda_x^+, \lambda_z^+) = (2390, 2400)$, and this streamwise wavelength corresponds to $\lambda_x/\delta_p = 3.8$. This is within the range of the characteristic wavelength of the K-H instability of $\lambda_x/\delta_p = 3$–5.5 [7,8,19], demonstrating the presence of the spanwise rollers for case 6x3z-thick. In addition, this implies that the characteristic of the spanwise roller is similar to that observed for turbulence over other types of porous media despite the fact that the size of the texture is considerably large and even comparable

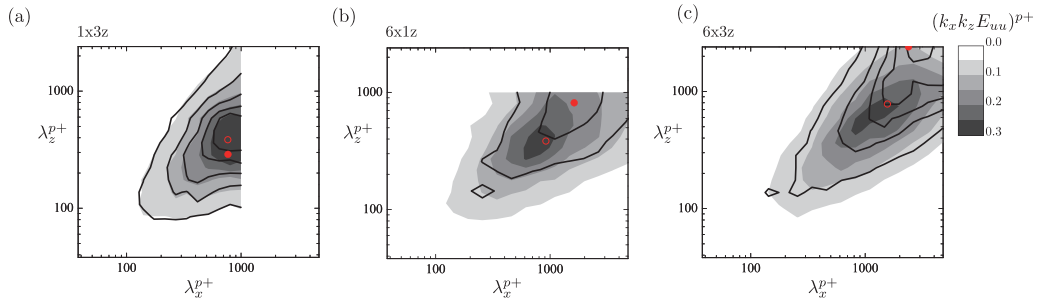

FIG. 6. Comparison of the one-dimensional streamwise premultiplied energy spectra of streamwise velocity fluctuations at $y^{p+} \simeq 10$ for (a) case 1x3z, (b) case 6x1z, and (c) case 6x3z. The contour line denotes the results for the thick porous wall cases. The shaded contour denotes the thin porous wall cases. The open and solid symbols indicate the maximum peak location of the spectra for the thin and thick porous wall cases.

to the channel height, i.e., $L = H/3$. For the spanwise-reduced domain case of 6x1z-thick, the streamwise wavelength for the maximum wavelength is $\lambda_x/\delta_p = 2.5$, which is slightly below the lower band of the proposed range for the spanwise rollers, $\lambda_x/\delta_p = 3$–5.5. This deviation may be attributed to the insufficient spanwise domain length for case 6x1z-thick. The periodic boundary conditions with the insufficient spanwise separation artificially increase the interaction of the spanwise rollers. The spectral analysis reveals that the spanwise rollers do not develop over thin porous walls, even for the spanwise-reduced domain case, demonstrating that sufficient vertical permeability, i.e., relaxation of wall blocking, is one of the necessary conditions for the development of spanwise rollers.

In summary, for the presently simulated cases, it was confirmed that the spanwise rollers develop only for cases 6x3z-thick and 6x1z-thick. In the following discussion, we will see how the spanwise rollers influence the turbulence statistics.

C. Standard turbulence statistics

Figure 7 shows profiles of the x-z plane-averaged streamwise mean velocity $\langle \overline{u} \rangle$ normalized by the average friction velocity u_τ. For comparison, the DNS data for a smooth wall at $\mathrm{Re}_\tau = 590$ from Vreman and Kuerten [63] are included. Note that this Re_τ value is comparable to the friction Reynolds number for a porous wall side for the present cases: $\mathrm{Re}_\tau^p = u_\tau^p \delta_p/\nu = 550$–$630$. The figure shows that for all cases, the profile of $\langle \overline{u} \rangle^+$ is lower than that of the smooth wall result and exhibits a strong asymmetry owing to the increased wall shear stress at a porous wall. In Fig. 7(a),

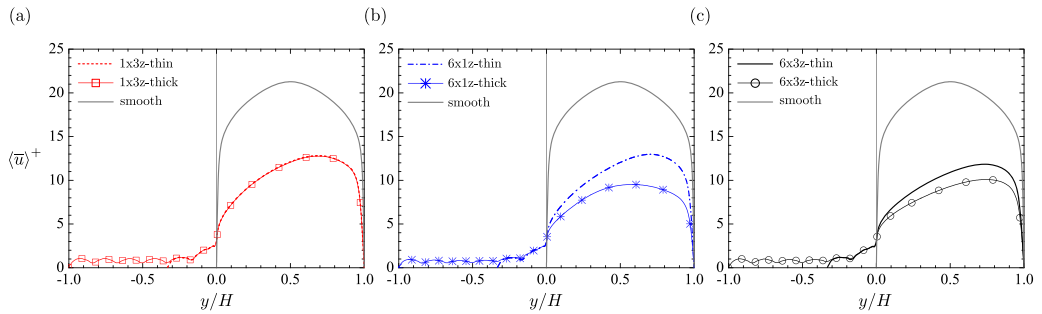

FIG. 7. Profiles of the streamwise mean velocity $\langle \overline{u} \rangle^+$: (a) streamwise-reduced domain cases (1x3z), (b) spanwise-reduced domain cases (6x1z), and (c) full-domain cases (6x3z). The DNS result for the smooth wall from Vreman and Kuerten [63] is included.

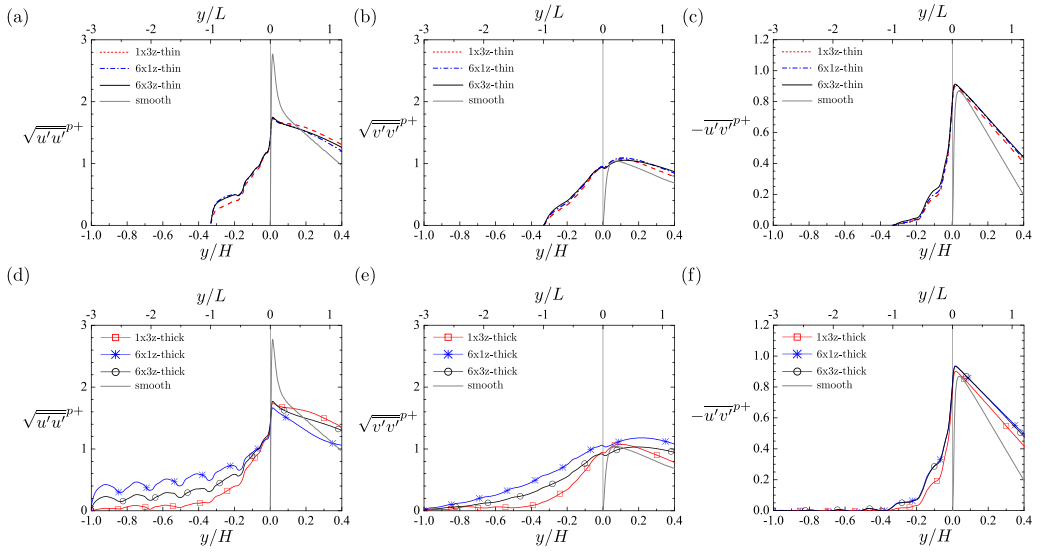

FIG. 8. Profiles of the Reynolds stresses around the porous wall: (a) streamwise component for thin porous wall cases, (b) wall-normal component for thin porous wall cases, (c) off-diagonal component for thin porous wall cases, (d) streamwise component for thick porous wall cases, (e) wall-normal component for thick porous wall cases, and (f) off-diagonal component for thick porous wall cases. The values are normalized by the friction velocity at the porous wall, u_τ^p.

for the streamwise-reduced domain cases (1x3z) where the spanwise roller is absent, the profiles for the thick and thin porous wall cases collapse perfectly, and the mean velocity profile is unaffected by the porous wall thickness. By contrast, for the spanwise-reduced cases (6x1z) in Fig. 7(b) and the full-domain cases (6x3z) in Fig. 7(c), the dependence of the porous wall thickness on $\langle\overline{u}\rangle^+$ is clearly visible. For both cases, the profile over the thick porous wall is lower than those over the thin porous wall, resulting from an increased skin friction coefficient at the porous wall, as observed earlier in Table I. Given that the spanwise rollers develop only for cases 6x1z-thick and 6x3z-thick, this modification is due to the role of the spanwise rollers.

To gain more insight into the effects of the domain size and porous wall thickness on turbulence, we focus on the Reynolds stress near the porous wall. Figure 8 shows profiles of the Reynolds stress components, which are normalized by the friction velocity at the porous wall u_τ^p. For comparison, the DNS data for a smooth wall at $\mathrm{Re}_\tau = 590$ from Vreman and Kuerten [63] are included. For the thin porous walls in Figs. 8(a)–8(c), the first notable observation is that the profiles near the thin porous walls are insensitive to the domain size. Interestingly, this observation may be similar to that reported by DNS studies of the minimum channel for rough-wall turbulent flows [61,64,65], which demonstrated that the hydraulic behavior near a rough surface predominantly depends on the roughness geometry and is not significantly affected by the width of the spanwise domain length as far as the spanwise domain is sufficiently large to fully immerse the representative single roughness element. Furthermore, the absence of the maximum peak value of the streamwise component in Fig. 8(a) maintaining the strength of the wall-normal component in Fig. 8(b) can also be found for the rough wall turbulent boundary layer [35,66–70]. These observations suggest that the thin porous wall under consideration is likely to behave as a rough wall.

For thick porous walls, as shown in Figs. 8(d)–8(f), the modification of the Reynolds stress appears qualitatively similar to that of the thin porous wall cases. However, the distinct disparity between the thin porous wall cases is that the domain size for the thick porous wall cases has a substantial influence on the Reynolds stress. Inside the porous wall ($y < 0$), the Reynolds normal

stresses in Figs. 8(d) and 8(e) are the largest for the spanwise-reduced domain case (6x1z), followed by the full-domain case (6x3z), and the smallest for the streamwise-reduced domain case (1x3z). Over the porous wall ($y > 0$) for cases 6x1z-thick and 6x3z-thick, the increase in the wall-normal component while decreasing the streamwise component is more prominent than the results for case 1x3z-thick. The increase in the wall-normal component around the porous wall is most likely a result of the spanwise rollers. Kuwata and Suga [17] reported that the spanwise rollers enhanced the pressure-velocity correlation terms, namely, the redistribution and pressure diffusion terms. The enhanced redistribution term over the porous wall increases the wall-normal Reynolds stress while decreasing the streamwise component, and the enhanced pressure diffusion term inside the porous wall transfers the energy over the porous wall toward deep inside the porous wall. Indeed, the increase in the wall-normal component is the most notable for case 6x1z-thick where the strong spanwise rollers are artificially induced by the periodic conditions with an insufficient separation as observed in Fig. 4.

Although the Reynolds normal stresses are sustained in Figs. 8(d) and 8(e), the Reynolds shear stress in Fig. 8(f) rapidly decays to zero in the first Kelvin cell layer of $-1 < y/L < 0$. This is because of the absence of the mean shear deep inside the porous wall. Note that, although a direct comparison is not shown here, the profiles for cases 1x3z-thick and 1x3z-thin are almost indistinguishable. That is, in the absence of the spanwise roller, an increase in wall thickness (i.e., increase in the vertical permeability) has no major influence on the near-wall turbulence.

D. Logarithmic mean velocity profiles

Although the previous section concentrates on the flow characteristics around and inside the porous wall, this section discusses the effects of the spanwise rollers on the flows in the logarithmic region. To this end, we introduce a modified logarithmic law, which is commonly used to characterize a streamwise mean velocity profile over a rough and/or porous wall:

$$\langle \overline{u} \rangle^+ = \frac{1}{\kappa} \ln\left(\frac{y+d}{h_r} \right), \tag{6}$$

where κ, d, and h_r are the von Kármán constant, zero-plane displacement, and equivalent roughness height, respectively. It is established that the introduction of parameters d and h_r yields a reasonably good representation of the mean velocity profile over a rough and/or porous wall. However, there are several possible choices for methods to determine the parameters. Specifically, concerning the value for κ, the universal value of $\kappa \simeq 0.4$ has been widely used in the field of vegetation canopies [71–74]. In contrast, Refs. [2,3,6,18,23] recommended a considerably lower value to better fit the logarithmic law profile, which was determined based on the diagnostic function γ:

$$\gamma = (y+d)^+ \frac{d\langle \overline{u} \rangle^+}{dy^+}. \tag{7}$$

In this procedure, the zero-plane displacement d is first determined such that the diagnostic function γ plateaus in the logarithmic region [2]. Once d is determined, κ is given as the inverse of the plateau value. Then, the equivalent roughness height h_r can finally be obtained by fitting Eq. (6) for the mean velocity profile. Manes *et al.* [23] and Suga *et al.* [3,19] reported that the parameters h_r and d were closely related to the characteristic length scale of the porous media such as the square root of the permeability. However, there is no universally accepted correlation function that estimates the full sets of these parameters for various porous media.

Another well-known approach to obtain the value of d is using the Jackson model [75]. In this approach, d is assumed to be the level at which the height-averaged drag force acts. Although this approach has been validated in turbulent flows over porous and rough walls [2,76,77], this approach was originally developed for the zero-pressure-gradient turbulent boundary layer. Hence, care should be taken when using this for flows subjected to a constant pressure difference. Otherwise, the momentum supply due to the pressure gradient in the porous wall affects the position of the center of

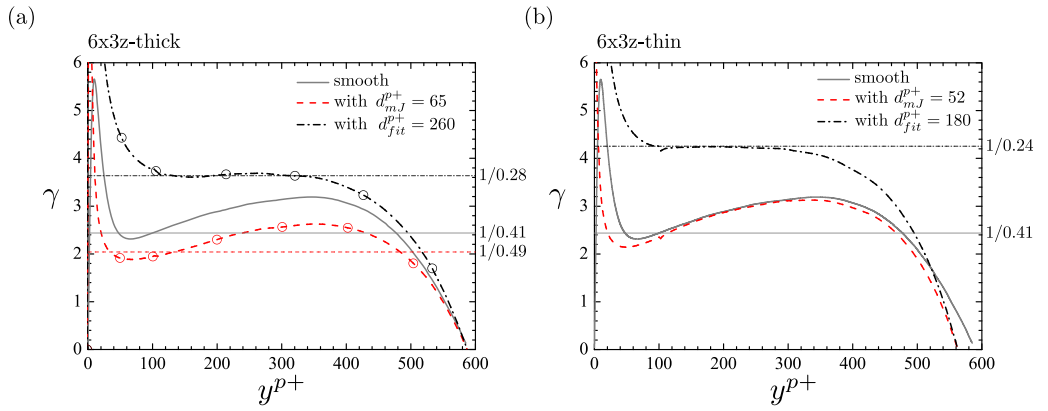

FIG. 9. Diagnostic function γ with the two definitions of the zero-plane displacements for (a) case 6x3z-thick and (b) case 6x3z-thin. Also shown is the DNS result for the smooth wall case at $\mathrm{Re}_\tau = 590$ from Vreman and Kuerten [63].

the drag [78]. In this study, the extended Jackson model proposed by Breugem *et al.* [2] is used for pressure-driven turbulent flow, and to assess the validity of the sets of logarithmic law parameters obtained by the two approaches, namely, the fitting method and extended Jackson model.

Following the extended Jackson model proposed by Breugem *et al.* [2] the zero-plane displacement is computed using the drag force f_x in spatial and Reynolds (double) averaged momentum equations for incompressible flow, which is expressed in the present flow system [79,80]:

$$0 = -\frac{\varphi}{\rho}\frac{\partial \langle \overline{p} \rangle^f}{\partial x} + \nu \frac{\partial}{\partial y}\left(\frac{\partial \langle \overline{u} \rangle}{\partial y}\right) - \frac{\partial}{\partial y}(\langle \overline{u'v'} \rangle + \langle \tilde{\overline{u}}\, \tilde{\overline{v}} \rangle) - \underbrace{\left(-\frac{\nu}{A}\int_L n_k \frac{\partial \tilde{\overline{u}}}{\partial x_k} d\ell + \frac{1}{\rho A}\int_L n_x \tilde{\overline{p}} d\ell\right)}_{f_x} - \underbrace{\nu \frac{\partial \varphi}{\partial y}\frac{\partial \langle \overline{u} \rangle^f}{\partial y}}_{g_x}, \tag{8}$$

where L represents the obstacle perimeter within an averaging x-z plane, ℓ represents the obstacle perimeter in the x-z plane, and n_k is its unit normal vector pointing outward from the fluid to the solid phase. The Reynolds- and plane-averaging operators produce two second moments, namely, the plane-averaged Reynolds shear stress $\langle \overline{u'v'} \rangle$ and plane-dispersive covariance $\langle \tilde{\overline{u}}\, \tilde{\overline{v}} \rangle$. The other terms arising inside the porous wall are the drag force term f_x and the additional viscous term g_x, which is related to the wall-normal gradient of plane porosity. From the expression for f_x in Eq. (8), the drag force represents the mean pressure and viscous forces offered by the porous media. In the extended Jackson model [2], zero-plane displacement is defined as the level at which the mean drag minus the mean pressure gradient acts as follows:

$$d_{mJ} = \frac{\int_{-h}^{0} y f_x^m dy}{\int_{-h}^{0} f_x^m dy}, \tag{9}$$

where f_x^m excludes the drag force due to the pressure-driven mean flow inside the porous wall,

$$f_x^m = f_x - \left(-\frac{\varphi}{\rho}\frac{\partial \langle \overline{p} \rangle^f}{\partial x}\right). \tag{10}$$

Figure 9 compares profiles of the diagnostic functions with d_{fit} and d_{mJ} for the full-domain cases of 6x3z-thick and 6x3z-thin. Here, d_{fit} is the zero-plane displacement determined by the fitting procedure proposed by Breugem *et al.* [2]. In addition, the DNS result for the smooth wall case at

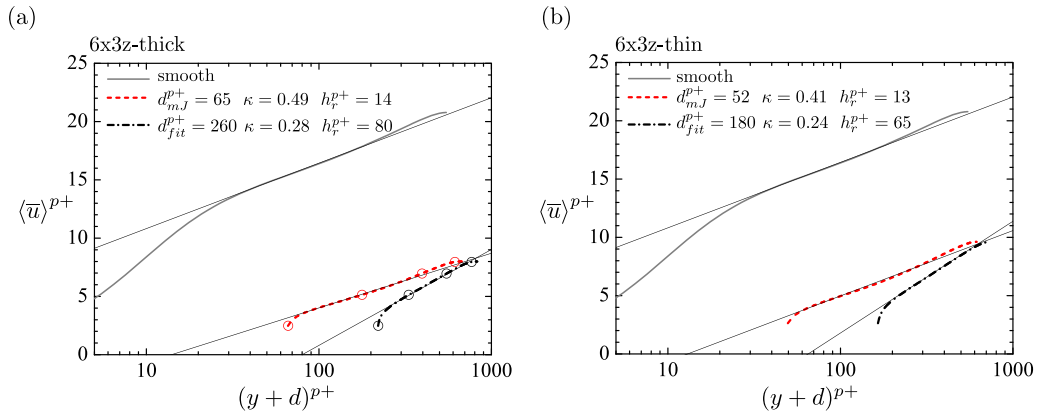

FIG. 10. Inner-scaled mean velocity profiles with the logarithmic scaling of $(y + d_{\text{fit}})^{p+}$ and $(y + d_{mJ})^{p+}$ for (a) case 6x3z-thick and (b) case 6x3z-thin. The logarithmic law profiles based on d_{fit} and d_{mJ} are also shown for comparison. The DNS result for the smooth wall case at $\text{Re}_\tau = 590$ from Vreman and Kuerten [63] is also plotted.

$\text{Re}_\tau = 590$ [63] is shown for comparison. The results for the reduced domain cases of 6x1z and 1x3z are not shown here because the logarithmic mean velocity profiles cannot be properly represented by the reduced domain cases. For the thick porous wall case in Fig. 9(a), γ with d_{mJ} is lower than that for the smooth wall case. Conversely, for the thin porous wall case in Fig. 9(b), γ with d_{mJ} agrees well with the smooth wall result in the region of $150 < y^{p+} < 350$. This demonstrates that the mean velocity profile with d_{mJ} for the thin porous wall case exhibits similarity to the smooth wall result in the logarithmic region. In other words, the thin porous wall has little effect on the flow in the logarithmic region. This may substantiate the outer layer similarity proposed by Townsend [81], who stated that the flows outside the roughness sublayer are independent of the surface condition, which was supported by many experimental studies [66,68,82]. However, it should be noted that the similarity hypothesis does not hold completely for the present flow because this hypothesis is satisfied only for a high Reynolds number flow over a sufficiently small roughness [83]. When we use d_{mJ}, the value of κ for the thin porous wall case is almost the same as that for the smooth wall value ($\kappa = 0.41$), while a somewhat larger value for $\kappa = 0.49$ may be expected for the thick porous wall case. The increase in κ for the thick porous wall cases may reflect the presence of the spanwise rollers as observed in Fig. 5, where we observe that the velocity fluctuations induced by the spanwise rollers dominate the core region.

On the other hand, when we focus on the profiles of γ with d_{fit}, the profiles of γ for thick and thin porous wall cases reach a plateau around $100 < y^{p+} < 200$ with a considerably larger d_{fit} value compared with d_{mJ}. The resultant κ values are 0.28 and 0.24 for the thick and thin porous wall cases, respectively, both of which are considerably lower than the standard value for the smooth wall case. This is consistent with the findings in Refs. [2,3,6,23]. The fitting approach is highly suited for discussing the experimental data because this approach does not require any flow information inside the porous wall that cannot be accessed by the experiments. However, considering the fact that the Reynolds number under consideration is not sufficiently high, the plateau value of γ may be just an outcome of overfitting to the logarithmic law. Indeed, Jiménez and Moser [84] and Lee and Moser [85] found that even for DNS data around $\text{Re}_\tau = 2000$, the diagnostic function did not reach a plateau and the mean velocity profiles did not exhibit a distinct logarithmic region.

The resulting inner-scaled mean velocity profiles with the logarithmic scaling of $(y + d_{\text{fit}})^{p+}$ and $(y + d_{mJ})^{p+}$ are shown in Fig. 10 along with the corresponding logarithmic law profiles of Eq. (6). For comparison, the DNS result for a smooth wall at $\text{Re}_\tau = 590$ is included. As expected in Fig. 9,

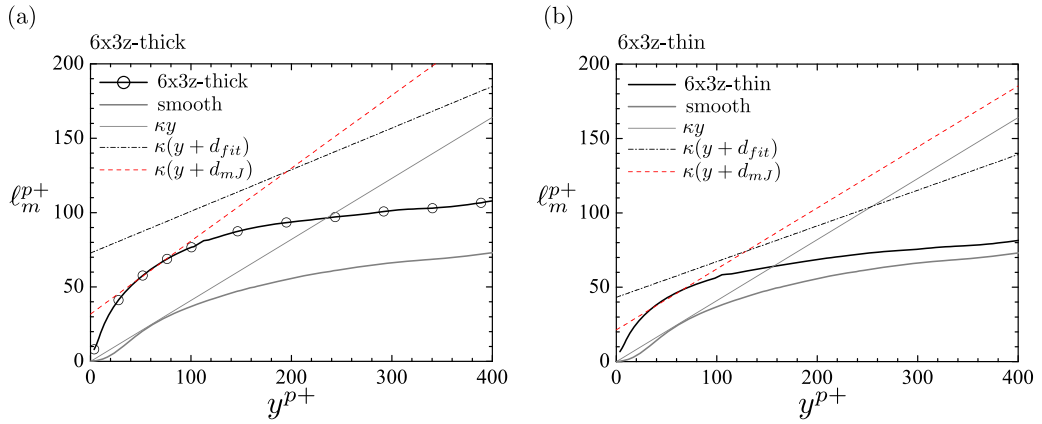

FIG. 11. Comparison of the mixing-length with the classical mixing-length model of $\ell_m = \kappa(y + d)$ for (a) case 6x3z-thick and (b) case 6x3z-thin. The DNS result for the smooth wall case at $\mathrm{Re}_\tau = 590$ from Vreman and Kuerten [63] is also plotted.

the mean velocity profile with d_{fit} perfectly follows the logarithmic law profile with a considerably steeper slope in comparison with the smooth wall case. Concerning the profiles with d_{mJ}, although the agreement is not perfect, the profile over the thin porous wall can be reasonably approximated by the logarithmic law profile with $\kappa = 0.41$, whereas a somewhat larger value of $\kappa = 0.49$ offers a good approximation for the velocity profile over the thick porous wall. The larger value of κ for the thick porous wall case is physically interpreted as the result of the spanwise rollers. It has been well established that the vortex size is directly related to Prandtl's classical mixing length, which scales with the distance from the wall with the proportional constant of κ. In the context of the turbulence over the thick porous wall, the turbulent flow is dominated by the spanwise rollers associated with the K-H instability as observed in Figs. 4 and 5; the characteristic vortex size for the thick porous wall appears to be larger than that for the thin porous wall, as observed in Figs. 4 and 5. The increase in the vortex size by the spanwise rollers means an increase in the mixing length, implying an increase in the proportional constant of the mixing length κ from the standard value of 0.41.

The earlier results show that the von Kármán constant strongly depends on the zero-plane displacement; d by the fitting approach yields considerably lower κ values than the standard value of $\kappa = 0.41$, whereas that by the extended Jackson model yields the same or a slightly higher value for κ. For a physical understanding of the modification of κ, I further discuss the von Kármán constant in terms of the mixing length defined as

$$\ell_m = -\langle \overline{u'v'} \rangle \Big/ \frac{d\langle \overline{u} \rangle}{dy}. \tag{11}$$

Figure 11 shows a comparison of ℓ_m with the classical mixing-length model (MLM) for a rough wall boundary layer where ℓ_m is proportional to the distance from the rough surface with the zero-plane displacement $\ell_m = \kappa(y + d)$ [58,86]. The growth of ℓ_m with respect to y is faster for the porous wall cases than that for the smooth wall case, and ℓ_m for the thick porous wall case in Fig. 11(a) is much larger than that for the thin porous wall case in Fig. 11(b). Both the MLMs with d_{fit} and d_{mJ} can reproduce the rapid growth of ℓ_m near the porous wall. However, the MLM with d_{fit} significantly overpredicts ℓ_m, whereas the accuracy of the MLM with d_{mJ} is better and comparable to that of the smooth wall case. Regarding the MLM with d_{mJ}, the rapid growth in ℓ_m near the thin porous wall [Fig. 11(b)], which is due to the nonzero turbulent eddy viscosity at the porous/fluid interface, is reasonably represented by the nonzero value of d_{mJ}, and a further increase in ℓ_m near the thick

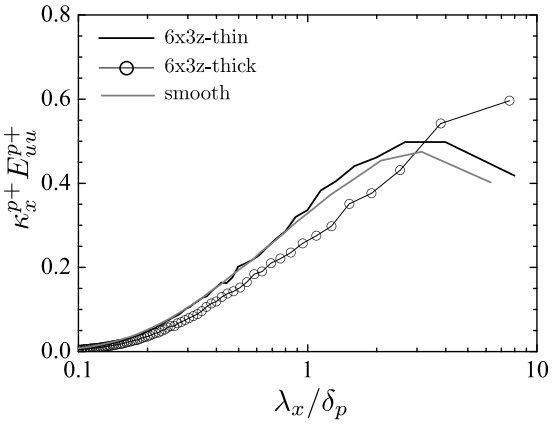

FIG. 12. Comparison of the one-dimensional premultiplied streamwise energy spectra in the middle of the boundary layer at $(y + d_{mJ})/\delta_p = 0.5$. The DNS result for the smooth wall case at $\mathrm{Re}_\tau = 590$ from Vreman and Kuerten [63] is also plotted.

porous wall [Fig. 11(a)] is represented not only by the nonzero value of d_{mJ} but also by the increased proportional constant of κ. Reasonably good agreement of ℓ_m with the increased κ near the thick porous wall in Fig. 11(a) supports the earlier explanation that the spanwise rollers increase the characteristic vortex size, i.e., the mixing length, leading to an increase in κ. Note that the simulated Reynolds number is not sufficiently high to discuss the logarithmic velocity profile. However, the above results suggest that the logarithmic law parameters based on the extended Jackson model may be valid in the sense that the set of the logarithmic law parameters provides a reasonable representation of the increase in the mixing length owing to the role of the spanwise rollers.

Finally, to better understand how the spanwise rollers affect the turbulence in the logarithmic region, Fig. 12 presents a comparison of the energy spectrum at $(y + d_{mJ})/\delta_p = 0.5$ for full-domain cases of 6x3z. Note that I consider the scaling of $(y + d_{mJ})/\delta_p$ because the outer layer similarity in the context of rough wall turbulence is usually discussed based on profiles with the virtual origin [87–90]. For comparison, the DNS result at $\mathrm{Re}_\tau = 590$ by Vreman and Kuerten [63] is included. In Fig. 12, the energy spectrum for the thin porous wall case generally agrees with that for the smooth wall case, suggesting that the effect of the thin porous wall is generally confined to the near-wall region. This observation is similar to what has been reported for rough wall turbulence, which is referred to as the outer layer similarity [81]. However, note that as the present rough wall occupies a relatively larger fraction of the boundary layer, the similarity in the logarithmic region does not completely hold [83], which may be the reason for the slight discrepancy with the smooth wall result. Conversely, for the thick porous wall case, the energy spectrum gains strength in the long-wavelength region of $\lambda_x/\delta_p > 3$, and the profile deviates largely from that for smooth wall case. This clearly indicates that the breakdown of the similarity in the logarithmic region as shown in Fig. 9 is due to the role of the relatively large-scale structures associated with the spanwise rollers caused by the K-H instability.

In summary, the turbulence over the thin porous wall is similar to the rough wall turbulence in the sense that the turbulence statistics are insensitive to the computational domain size (see Sec. IV C), and the similarity in the logarithmic region is preserved. Thus, the turbulence over the thin porous wall is categorized as rough wall turbulence rather than porous wall turbulence. This suggests that near-wall turbulent motions, including streaks and longitudinal vortices, are predominantly altered by the surface roughness in the absence of the spanwise rollers, whereas the vertical permeability indirectly affects the near-wall turbulent motions through the spanwise rollers associated with the K-H instability.

V. CONCLUSIONS

The influence of spanwise rollers associated with K-H instability on a turbulent flow over a porous wall was systematically studied using DNSs of porous-walled channel flows with constraints in the size of the computational domain. In addition to the full computational domain, the streamwise-reduced and spanwise-reduced domains were considered, both of which were designed such that they were large enough to sustain the near-wall turbulence including the streaks and longitudinal vortices but too small to properly capture spanwise rollers by the K-H instability. For each domain case, we considered thick and thin porous walls for the bottom wall to discuss the effect of vertical permeability.

Near-wall turbulent motions, including streaks and longitudinal vortices, are found to be insensitive to vertical permeability. This suggests that the modification of these motions is principally due to the surface roughness of the porous wall. The vertical permeability is found to allow the development of spanwise rollers with streamwise alternating low- and high-speed regions. The spanwise rollers contribute to the enhancement of the turbulence inside a porous wall, leading to an increase in the skin friction coefficient at the porous wall. To discuss the mean flow away from a porous wall, we discuss the logarithmic mean velocity with two commonly used definitions of zero-plane displacement. The fitting approach, in which the zero-plane displacement is obtained by fitting the mean velocity profile to the logarithmic law, yields a considerably smaller von Kármán constant, irrespective of the presence of spanwise rollers. By contrast, the discussion based on the modified Jackson model, which is an extended version of the Jackson model for pressure-driven turbulent boundary layers, leads to completely different conclusions. For a thin porous wall in which spanwise rollers do not develop, the von Kármán constant is the same as that for a smooth wall. The similarity in the logarithmic region can also be found in the energy spectra. This is one of the manifestations of rough wall turbulence. Hence, a thin porous wall is considered to behave as a rough wall rather than a porous wall. For the thick porous wall case, the von Kármán constant is increased by 20%. This is considered to reflect an increase in the characteristic vortex size owing to the spanwise rollers. Indeed, the mixing length is substantially larger than that for smooth wall turbulence, and this can be reasonably predicted using the classical mixing-length model with an increased von Kármán constant. The discussion based on the modified Jackson model offers physical understanding in the sense that the obtained von Kármán constant reasonably reflects the modification of the characteristic vortex size owing to the spanwise roller.

A series of constrained DNSs reveals the role of spanwise rollers by the K-H instability in a porous wall turbulence. However, owing to limited computational resources, the present DNSs only consider one type of isotropic porous medium at a single Reynolds number. It is important to discuss a sufficiently high Reynolds number flow in which the logarithmic scaling of the mean velocity is possible, as well as the effects of the porous medium characteristics on the spanwise roller. This is beyond the scope of this paper, however, and will be the focus of a future study.

ACKNOWLEDGMENTS

The author expresses gratitude to Dr. K. Suga and Dr. M. Kaneda for their support. This study was partly financially supported by a research grant (Grant No. 19H02069) from JSPS Japan. The numerical calculations were carried out on the TSUBAME3.0 supercomputer in the Tokyo Institute of Technology in research projects (ID hp210006).

[1] H. Darcy, Les fontaines publiques de la ville de dijon, Dalmont, Paris (1856).

[2] W. P. Breugem, B. J. Boersma, and R. E. Uittenbogaard, The influence of wall permeability on turbulent channel flow, J. Fluid Mech. **562**, 35 (2006).

[3] K. Suga, Y. Matsumura, Y. Ashitaka, S. Tominaga, and M. Kaneda, Effects of wall permeability on turbulence, Int. J. Heat Fluid Flow **31**, 974 (2010).
[4] K. Suga, M. Mori, and M. Kaneda, Vortex structure of turbulence over permeable walls, Int. J. Heat Fluid Flow **32**, 586 (2011).
[5] C. Manes, D. Poggi, and L. Ridol, Turbulent boundary layers over permeable walls: Scaling and near-wall structure, J. Fluid Mech. **687**, 141 (2011).
[6] Y. Kuwata and K. Suga, Lattice Boltzmann direct numerical simulation of interface turbulence over porous and rough walls, Int. J. Heat Fluid Flow **61**, 145 (2016).
[7] Y. Kuwata and K. Suga, Direct numerical simulation of turbulence over anisotropic porous media, J. Fluid Mech. **831**, 41 (2017).
[8] Y. Kuwata and K. Suga, Extensive investigation of the influence of wall permeability on turbulence, Int. J. Heat Fluid Flow **80**, 108465 (2019).
[9] G. Gómez-de-Segura, A. Sharma, and R. García-Mayoral, Turbulent drag reduction using anisotropic permeable substrates, Flow Turbul. Combust. **100**, 995 (2018).
[10] M. E Rosti, L. Brandt, and A. Pinelli, Turbulent channel flow over an anisotropic porous wall-drag increase and reduction, J. Fluid Mech. **842**, 381 (2018).
[11] M. R. Raupach, P. A. Coppin, and B. J. Legg, Experiments on scalar dispersion within a model plant canopy part I: The turbulence structure, Boundary-Layer Meteorol. **35**, 21 (1986).
[12] M. R. Raupach, J. J. Finnigan, and Y. Brunet, Coherent eddies and turbulence in vegetation canopies: The mixing-layer analogy, Boundary-Layer Meteorol. **78**, 351 (1996).
[13] J. Finnigan, Turbulence in plant canopies, Annu. Rev. Fluid Mech. **32**, 519 (2000).
[14] B. L. White and H. M. Nepf, Shear instability and coherent structures in shallow flow adjacent to a porous layer, J. Fluid Mech. **593**, 1 (2007).
[15] J. Jimenez, M. Uhlmann, A. Pinelli, and G. Kawahara, Turbulent shear flow over active and passive porous surfaces, J. Fluid Mech. **442**, 89 (2001).
[16] G. Gómez-de-Segura and R. García-Mayoral, Turbulent drag reduction by anisotropic permeable substrates—analysis and direct numerical simulations, J. Fluid Mech. **875**, 124 (2019).
[17] Y. Kuwata and K. Suga, Transport mechanism of interface turbulence over porous and rough walls, Flow Turbul. Combust. **97**, 1071 (2016).
[18] X. Chu, W. Wang, G. Yang, A. Terzis, R. Helmig, and B. Weigand, Transport of turbulence across permeable interface in a turbulent channel flow: Interface-resolved direct numerical simulation, Transp. Porous Media **136**, 165 (2021).
[19] K. Suga, Y. Okazaki, U. Ho, and Y. Kuwata, Anisotropic wall permeability effects on turbulent channel flows, J. Fluid Mech. **855**, 983 (2018).
[20] A. B. Shvidchenko and G. Pender, Macroturbulent structure of open-channel flow over gravel beds, Water Resour. Res. **37**, 709 (2001).
[21] A. G. Roy, T. Buffin-Belanger, H. Lamarre, and A. D. Kirkbride, Size, shape and dynamics of large-scale turbulent flow structures in a gravel-bed river, J. Fluid Mech. **500**, 1 (2004).
[22] H. M. Nepf and E. R. Vivoni, Flow structure in depth-limited, vegetated flow, J. Geophys. Res. Oceans **105**, 28547 (2000).
[23] C. Manes, D. Pokrajac, I. McEwan, and V. Nikora, Turbulence structure of open channel flows over permeable and impermeable beds: A comparative study, Phys. Fluids **21**, 125109 (2009).
[24] D. Pokrajac and C. Manes, Velocity measurements of a free-surface turbulent flow penetrating a porous medium composed of uniform-size spheres, Transp. Porous Media **78**, 367 (2009).
[25] P. Lammers, K. N. Beronov, R. Volkert, G. Brenner, and F. Durst, Lattice BGK direct numerical simulation of fully developed turbulence in incompressible plane channel flow, Comput. Fluids **35**, 1137 (2006).
[26] K. Suga, Y. Kuwata, K. Takashima, and R. Chikasue, A D3Q27 multiple-relaxation-time lattice Boltzmann method for turbulent flows, Comput. Math. Appl. **69**, 518 (2015).
[27] M. Gehrke, C. F. Janßen, and T. Rung, Scrutinizing lattice Boltzmann methods for direct numerical simulations of turbulent channel flows, Comput. Fluids **156**, 247 (2017).
[28] C. K. Aidun and J. R. Clausen, Lattice-Boltzmann method for complex flows, Annu. Rev. Fluid Mech. **42**, 439 (2010).

[29] X. Wang and T. Aoki, High performance computation by multi-node GPU cluster-Tsubame2.0 on the air flow in an urban city using lattice Boltzmann method, Int. J. Aero. Lightweight Struct. (IJALS) **2**, 77 (2012).
[30] N. Onodera, T. Aoki, T. Shimokawabe, and H. Kobayashi, Large-scale LES wind simulation using lattice Boltzmann method for a 10 km× 10 km area in metropolitan Tokyo, Tsubame ESJ **9**, 2 (2013).
[31] M. Hasert, J. Bernsdorf, and S. Roller, Lattice Boltzmann simulation of non-Darcy flow in porous media, Proc. Comput. Sci. **4**, 1048 (2011).
[32] M. Krafczyk, K. Kucher, Y. Wang, and M. Geier, DNS/LES studies of turbulent flows based on the cumulant lattice Boltzmann approach, in *High Performance Computing in Science and Engineering 14* (Springer, Berlin, 2015), pp. 519–531.
[33] G. Tóth and I. M. Jánosi, Vorticity generation by rough walls in 2D decaying turbulence, J. Stat. Phys. **161**, 1508 (2015).
[34] Y. Jin, M. F. Uth, and H. Herwig, Structure of a turbulent flow through plane channels with smooth and rough walls: An analysis based on high resolution DNS results, Comput. Fluids **107**, 77 (2015).
[35] Y. Kuwata and Y. Kawaguchi, Direct numerical simulation of turbulence over systematically varied irregular rough surfaces, J. Fluid Mech. **862**, 781 (2019).
[36] P. Eichler, V. Fuka, and R. Fučík, Cumulant lattice Boltzmann simulations of turbulent flow above rough surfaces, Comput. Math. Appl. **92**, 37 (2021).
[37] L.-P. Wang, O. Ayala, H. Gao, C. Andersen, and K. L. Mathews, Study of forced turbulence and its modulation by finite-size solid particles using the lattice Boltzmann approach, Comput. Math. Appl. **67**, 363 (2014).
[38] A. Eshghinejadfard, A. Abdelsamie, S. A. Hosseini, and D. Thevenin, Immersed boundary lattice Boltzmann simulation of turbulent channel flows in the presence of spherical particles, Int. J. Multiphase Flow **96**, 161 (2017).
[39] G. Wang, D. Wan, C. Peng, K. Liu, and L.-P. Wang, LBM study of aggregation of monosized spherical particles in homogeneous isotropic turbulence, Chem. Eng. Sci. **201**, 201 (2019).
[40] Y. Kuwata and R. Nagura, Direct numerical simulation on the effects of surface slope and skewness on rough-wall turbulence, Phys. Fluids **32**, 105113 (2020).
[41] Y. Kuwata, T. Sugiyama, and Y. Kawaguchi, On the scaling of turbulence over an irregular rough surface in a transitionally rough regime, J. Therm. Sci. Tech. **15**, JTST0015 (2020).
[42] Y. Kuwata, K. Tsuda, and K. Suga, Direct numerical simulation of turbulent conjugate heat transfer in a porous-walled duct flow, J. Fluid Mech. **904**, A9 (2020).
[43] W. Thomson, LXIII, On the division of space with minimum partitional area, London, Edinburgh, Dublin Philos. Mag. J. Sci. **24**, 503 (1887).
[44] M. Chandesris, A. D'Hueppe, B. Mathieu, D. Jamet, and B. Goyeau, Direct numerical simulation of turbulent heat transfer in a fluid-porous domain, Phys. Fluids **25**, 125110 (2013).
[45] J. Jiménez and P. Moin, The minimal flow unit in near-wall turbulence, J. Fluid Mech. **225**, 213 (1991).
[46] A. Busse and N. D. Sandham, Parametric forcing approach to rough-wall turbulent channel flow, J. Fluid Mech. **712**, 169 (2012).
[47] Y. Kuwata and Y. Kawaguchi, Direct numerical simulation of turbulence over resolved and modelled rough walls with irregularly distributed roughness, Int. J. Heat Fluid Flow **77**, 1 (2019).
[48] J. T. Richardson, Y. Peng, and D. Remue, Properties of ceramic foam catalyst supports: Pressure drop, Appl. Catal. A **204**, 19 (2000).
[49] W. Xu, H. Zhang, Z. Yang, and J. Zhang, Numerical investigation on the flow characteristics and permeability of three-dimensional reticulated foam materials, Chem. Eng. J. **140**, 562 (2008).
[50] Z. Nie, Y. Lin, and Q. Tong, Modeling structures of open cell foams, Comput. Mater. Sci. **131**, 160 (2017).
[51] A. Inayat, H. Freund, T. Zeiser, and W. Schwieger, Determining the specific surface area of ceramic foams: The tetrakaidecahedra model revisited, Chem. Eng. Sci. **66**, 1179 (2011).
[52] F. Lucci, A. Della Torre, J. von Rickenbach, G. Montenegro, D. Poulikakos, and P. D. Eggenschwiler, Performance of randomized kelvin cell structures as catalytic substrates: Mass-transfer based analysis, Chem. Eng. Sci. **112**, 143 (2014).

[53] A. Bhattacharya, V. V. Calmidi, and R. L. Mahajan, Thermophysical properties of high porosity metal foams, Int. J. Heat Mass Transfer **45**, 1017 (2002).
[54] Y. Kuwata and K. Suga, Imbalance-correction grid-refinement method for lattice Boltzmann flow simulations, J. Comput. Phys. **311**, 348 (2016).
[55] Y. Kuwata, Direct numerical simulation of turbulent heat transfer on the Reynolds analogy over irregular rough surfaces, Int. J. Heat Fluid Flow **92**, 108859 (2021).
[56] M. E. Rosti, L. Cortelezzi, and M. Quadrio, Direct numerical simulation of turbulent channel flow over porous walls, J. Fluid Mech. **784**, 396 (2015).
[57] W.-P. Breugem and B.-J. Boersma, Direct numerical simulations of turbulent flow over a permeable wall using a direct and a continuum approach, Phys. Fluids **17**, 025103 (2005).
[58] D. Poggi, A. Porporato, L. Ridolfi, J. D. Albertson, and G. G. Katul, The effect of vegetation density on canopy sub-layer turbulence, Boundary-Layer Meteorol. **111**, 565 (2004).
[59] S. Toh and T. Itano, Interaction between a large-scale structure and near-wall structures in channel flow, J. Fluid Mech. **524**, 249 (2005).
[60] O. Flores and J. Jiménez, Hierarchy of minimal flow units in the logarithmic layer, Phys. Fluids **22**, 071704 (2010).
[61] M. MacDonald, D. Chung, N. Hutchins, L. Chan, A. Ooi, and R. García-Mayoral, The minimal-span channel for rough-wall turbulent flows, J. Fluid Mech. **816**, 5 (2017).
[62] H. Abe, R. A. Antonia, and S. Toh, Large-scale structures in a turbulent channel flow with a minimal streamwise flow unit, J. Fluid Mech. **850**, 733 (2018).
[63] A. W. Vreman and J. G. M. Kuerten, Statistics of spatial derivatives of velocity and pressure in turbulent channel flow, Phys. Fluids **26**, 085103 (2014).
[64] D. Chung, L. Chan, M. MacDonald, N. Hutchins, and A. Ooi, A fast direct numerical simulation method for characterising hydraulic roughness, J. Fluid Mech. **773**, 418 (2015).
[65] M. MacDonald, N. Hutchins, and D. Chung, Roughness effects in turbulent forced convection, J. Fluid Mech. **861**, 138 (2019).
[66] P. M. Ligrani and R. J. Moffat, Structure of transitionally rough and fully rough turbulent boundary layers, J. Fluid Mech. **162**, 69 (1986).
[67] P.-Å. Krogstadt and R. A. Antonia, Surface roughness effects in turbulent boundary layers, Exp. Fluids **27**, 450 (1999).
[68] K. A. Flack, M. P. Schultz, and T. A. Shapiro, Experimental support for Townsend's Reynolds number similarity hypothesis on rough walls, Phys. Fluids **17**, 035102 (2005).
[69] A. Busse, M. Lützner, and N. D. Sandham, Direct numerical simulation of turbulent flow over a rough surface based on a surface scan, Comput. Fluids **116**, 129 (2015).
[70] P. Forooghi, A. Stroh, P. Schlatter, and B. Frohnapfel, Direct numerical simulation of flow over dissimilar, randomly distributed roughness elements: A systematic study on the effect of surface morphology on turbulence, Phys. Rev. Fluids **3**, 044605 (2018).
[71] Y. Brunet, J. J. Finnigan, and M. R. Raupach, A wind tunnel study of air flow in waving wheat: Single-point velocity statistics, Boundary-Layer Meteorol. **70**, 95 (1994).
[72] M. R. Raupach, Simplified expressions for vegetation roughness length and zero-plane displacement as functions of canopy height and area index, Boundary-Layer Meteorol. **71**, 211 (1994).
[73] I. Nezu and M. Sanjou, Turbulence structure and coherent motion in vegetated canopy open-channel flows, J. Hydro-Environ. Res. **2**, 62 (2008).
[74] H. M. Nepf, Flow and transport in regions with aquatic vegetation, Annu. Rev. Fluid Mech. **44**, 123 (2012).
[75] P. S. Jackson, On the displacement height in the logarithmic velocity profile, J. Fluid Mech. **111**, 15 (1981).
[76] S. Leonardi, P. Orlandi, R. J. Smalley, L. Djenidi, and R. A. Antonia, Direct numerical simulations of turbulent channel flow with transverse square bars on one wall, J. Fluid Mech. **491**, 229 (2003).
[77] S. Leonardi and I. P. Castro, Channel flow over large cube roughness: A direct numerical simulation study, J. Fluid Mech. **651**, 519 (2010).

[78] D. Pokrajac, J. J. Finnigan, C. Manes, I. McEwan, and V. Nikora, On the definition of the shear velocity in rough bed open channel flows, in *River Flow*, Vol. 1 (Taylor & Francis, 2006), pp. 89–98.
[79] S. Whitaker, Flow in porous media I: A theoretical derivation of Darcy's law, Transp. Porous Media **1**, 3 (1986).
[80] S. Whitaker, The Forchheimer equation: A theoretical development, Transp. Porous Media **25**, 27 (1996).
[81] A. A. Townsend, *The Structure of Turbulent Shear Flow* (Cambridge University Press, Cambridge, UK, 1980).
[82] G. J. Kunkel and I. Marusic, Study of the near-wall-turbulent region of the high-Reynolds-number boundary layer using an atmospheric flow, J. Fluid Mech. **548**, 375 (2006).
[83] J. Jiménez, Turbulent flows over rough walls, Annu. Rev. Fluid Mech. **36**, 173 (2004).
[84] J. Jiménez and R. D. Moser, What are we learning from simulating wall turbulence? Philos. Trans. R. Soc. A **365**, 715 (2007).
[85] M. Lee and R. D. Moser, Direct numerical simulation of turbulent channel flow up to $\mathrm{Re}_\tau \approx 5200$, J. Fluid Mech. **774**, 395 (2015).
[86] G. G. Katul, L. Mahrt, D. Poggi, and C. Sanz, One- and two-equation models for canopy turbulence, Boundary-Layer Meteorol. **113**, 81 (2004).
[87] I. P. Castro, Rough-wall boundary layers: Mean flow universality, J. Fluid Mech. **585**, 469 (2007).
[88] L. Chan, M. MacDonald, D. Chung, N. Hutchins, and A. Ooi, A systematic investigation of roughness height and wavelength in turbulent pipe flow in the transitionally rough regime, J. Fluid Mech. **771**, 743 (2015).
[89] P. Forooghi, A. Stroh, F. Magagnato, S. Jakirlić, and B. Frohnapfel, Toward a universal roughness correlation, J. Fluids Eng. **139**, 121201 (2017).
[90] M. Thakkar, A. Busse, and N. D. Sandham, Surface correlations of hydrodynamic drag for transitionally rough engineering surfaces, J. Turbul. **18**, 138 (2017).